δf Monte Carlo calculation of neoclassical transport in perturbed tokamaks

Kimin Kim,[1] Jong-Kyu Park,[1] Gerrit J. Kramer,[1] and Allen H. Boozer[2]
[1]*Princeton Plasma Physics Laboratory, Princeton, New Jersey 08543, USA*
[2]*Columbia University, New York, New York 10027, USA*

(Received 9 April 2012; accepted 17 July 2012; published online 1 August 2012)

Non-axisymmetric magnetic perturbations can fundamentally change neoclassical transport in tokamaks by distorting particle orbits on deformed or broken flux surfaces. This so-called non-ambipolar transport is highly complex, and eventually a numerical simulation is required to achieve its precise description and understanding. A new δf particle orbit code (POCA) has been developed for this purpose using a modified pitch-angle collision operator preserving momentum conservation. POCA was successfully benchmarked for neoclassical transport and momentum conservation in the axisymmetric configuration. Non-ambipolar particle flux is calculated in the non-axisymmetric case, and the results show a clear resonant nature of non-ambipolar transport and magnetic braking. Neoclassical toroidal viscosity (NTV) torque is calculated using anisotropic pressures and magnetic field spectrum, and compared with the combined and $1/\nu$ NTV theory. Calculations indicate a clear δB^2 scaling of NTV, and good agreement with the theory on NTV torque profiles and amplitudes depending on collisionality.
 [http://dx.doi.org/10.1063/1.4740511]

I. INTRODUCTION

Non-axisymmetric magnetic perturbations can fundamentally change neoclassical transport in tokamaks by distorting particle orbits on deformed or broken flux surfaces.[1,2] Understanding transport under the non-axisymmetric magnetic perturbations is a critical issue for ITER (Ref. 3) and future fusion devices where the non-axisymmetric perturbations are potentially important control elements to actively stabilize locked modes, edge localized modes, and resistive wall modes.[4–8] The neoclassical transport in non-axisymmetry, often called neoclassical toroidal viscosity (NTV) transport in tokamaks, is intrinsically non-ambipolar,[9] and highly complex depending on parametric regimes. Progress has been substantially made by various analytical attempts,[10–14] but the analytic studies were limited in narrow regimes or strong approximations on particle orbits, geometries, and collisions. Therefore, a numerical approach with more realistic physics models is eventually required to achieve a precise and self-consistent description by directly following complex guiding-center orbits of particles without any approximation. This paper reports a development of new δf particle code for this purpose and successful calculations of the non-ambipolar transport and NTV torque in perturbed tokamaks.

A new δf particle code, POCA (Particle Orbit Code for Anisotropic pressures) has been developed for transport study in perturbed tokamaks. POCA aims to calculate fundamental properties of the neoclassical transport with the non-axisymmetric magnetic perturbations and to efficiently provide viable information to a 3D equilibrium solver. POCA follows guiding-center particle motions on the flux coordinates and solves Fokker-Planck equation with δf Monte Carlo method to obtain a perturbed distribution function δf. Collisions are calculated using a modified pitch-angle scattering collision operator, in which a momentum restoring term is included to conserve toroidal momentum. POCA is a local code which calculates the particle transport at a single flux surface, so it is more efficient than global code. In addition, δf Monte Carlo method applied to POCA is much more efficient than standard Monte Carlo method by a factor of 10^4,[15,16] which means the δf code requires less particles by a factor of 10^{-4} than the standard Monte Carlo code to achieve the same accuracy. These features will enable us to efficiently obtain the precise solutions of 3D neoclassical transport, as well as to couple and integrate them to a 3D equilibrium solver[17] by providing the anisotropic pressure tensor in the future.

For application of POCA, we will first verify its convergence and momentum conserving property and perform benchmarking of diffusion and bootstrap current with neoclassical theories and other numerical simulations in the axisymmetric configurations. In the non-axisymmetric configurations, we will show non-ambipolar transport calculations and a clear resonant nature of the transport and magnetic braking. Then, we will present benchmarking in the non-axisymmetric configuration with analytic theories, such as a combined formula and $1/\nu$ formula. Good agreements will be shown on NTV torque profiles and amplitudes depending on collisionality. Possible explanations on the discrepancies between POCA and the theories will be suggested, and effects of collision model, regime separation by collisionality, and Maxwellian energy distribution on the NTV calculation will be finally discussed.

This paper is organized as follows: in Sec. II, theoretical formulations and numerical implementation for δf Monte Carlo method are introduced. Benchmarking tests against neoclassical theory and simulations are described in Sec. III. In Sec. IV, non-ambipolar transport in the presence of non-axisymmetric magnetic perturbations is calculated and analyzed by applying an analytic magnetic perturbation model.

Section V describes NTV torque calculation by POCA and comparison results with NTV theories. Summary will be given in Sec. VI.

II. δf MONTE CARLO METHOD FOR NEOCLASSICAL TRANSPORT CALCULATION

In this section, we will describe theoretical formulations of the Fokker-Planck equation, collision operator, Hamiltonian equations of motion, and their technical implementations. Note that δf Monte Carlo method employed in POCA is based on the drift-kinetic equation, thus gyrating particle orbit is a gyro-averaged guiding-center motion. For this study, ion guiding-center motion is tested and solved since the non-ambipolar transport is dominated by ion transport.[9,12] Only ion-ion collisions are considered for collisions due to sub-dominance of ion-electron collisions.

A. Fokker-Planck equation

We start from Fokker-Planck equation,

$$\frac{df}{dt} = \frac{\partial f}{\partial t} + \vec{v}\cdot\frac{\partial f}{\partial \vec{x}} + \frac{\vec{F}}{m}\cdot\frac{\partial f}{\partial \vec{v}} = C(f). \tag{1}$$

Distribution function f can be written as $f = f_M \exp(\hat{f})$, where $\hat{f}$ is a deviation from local Maxwellian f_M. The distribution function can be further approximated to $f \approx f_M(1+\hat{f})$ since typically $\hat{f} \ll 1$ in fusion plasmas. The Fokker-Planck equation can be rewritten using the approximation as

$$\frac{d\ln f_M}{dt} + \frac{d\hat{f}}{dt} = C_m(f), \tag{2}$$

where $C_m(f)$ is a collision operator defined by $C_m(f) = C(f)/f$.

The Fokker-Planck equation is more convenient to solve with δf Monte Carlo method when it is expressed in terms of $\hat{f}$ rather than f. Neglecting external force term $\vec{F}$ in Eq. (1) and using the local Maxwellian, which is a function of toroidal flux and energy, the Fokker-Planck equation is reduced to

$$\frac{d\hat{f}}{dt} = -\vec{v}\cdot\vec{\nabla}\psi\frac{\partial \ln f_M}{\partial \psi} + C_m(\hat{f}), \tag{3}$$

where ψ is the toroidal flux. It is indicated in Eq. (3) that the deviation from Maxwellian, $\hat{f}$ is proportional to the displacement of particles from home flux surface, ψ_0 where the test particles are initially distributed. Therefore, $\hat{f}$ can be obtained by tracking the guiding-center motions of test particles with proper calculation of the collision term $C_m(\hat{f})$.

B. Collision operator

A modified pitch-angle scattering collision operator, which is composed of Lorentz collision operator and a momentum restoring term, is used to calculate the collision term in Eq. (3) and to preserve the conservation of the toroidal momentum. Energy scattering is neglected for computational efficiency and simplicity but can be included in the future upgrade.

The original Lorentz collision operator representing the pitch-angle scattering has a following form:

$$C(f) = \frac{\nu}{2}\frac{\partial}{\partial\lambda}\left[(1-\lambda^2)\frac{\partial f}{\partial\lambda}\right], \tag{4}$$

where λ is the particle pitch defined by $\lambda = v_\parallel/v$ with the parallel velocity along the magnetic field line $v_\parallel$ and ν is the collision frequency. The Lorentz collision operator in Eq. (4) conserves energy but does not conserve the toroidal momentum. An additional term is required to conserve the momentum, which restores the momentum lost by collisions. One form of the momentum conserving pitch-angle collision operator is given by Rosenbluth *et al.*[18] and Boozer and Gardner[19] as

$$C_{m.c.}(f) = \nu\frac{m}{B}v_\parallel\frac{\partial}{\partial\mu}\left[\mu\left(v_\parallel\frac{\partial f}{\partial\mu} + \frac{uB}{T}f\right)\right], \tag{5}$$

where B is the magnetic field, μ is the magnetic moment, and T is the temperature. The collision operator in Eq. (5) can be written as

$$C_{m.c.}(f) = \frac{\nu}{2}\frac{\partial}{\partial\lambda}\left[(1-\lambda^2)\left(\frac{\partial f}{\partial\lambda} - 3\frac{u}{v}f\right)\right], \tag{6}$$

by using $\mu = mv_\perp^2/2B$ and $T = 2/3\,E$. Here, u is the mean flow velocity defined by

$$u = \frac{1}{2}\int \hat{f} v_\parallel d\lambda. \tag{7}$$

A practical form of the momentum conserving collision operator, $C_{m.c.}(f)$ is obtained as a function of $\hat{f}$ by partial derivatives and ignoring subdominant terms[20] as

$$C_{m.c.}(\hat{f}) = \frac{\nu}{2}\frac{\partial}{\partial\lambda}\left[(1-\lambda^2)\frac{\partial\hat{f}}{\partial\lambda}\right] + 3\nu\frac{u}{v}\lambda. \tag{8}$$

Now the momentum conserving operator can be implemented by two steps. First, the particle pitch, λ is updated using a Monte Carlo equivalent of the original Lorentz collision operator in Eq. (4) by

$$\lambda_{new} = \lambda_{old}(1-\nu\tau) \pm [(1-\lambda_{old}^2)\nu\tau]^{1/2}, \tag{9}$$

where τ is a size of time step.[21] The symbol $\pm$ indicates that the sign is statistically determined by uniformly generated random number. The next step is to bring the momentum restoring term $3\nu(v/u)\lambda$ of Eq. (6) into the right hand side of Eq. (3). Then, $\hat{f}$ is calculated as following:

$$\Delta\hat{f} = -\Delta\psi\frac{\partial \ln f_M}{\partial\psi} + 3\nu\frac{u}{v}\lambda\tau, \tag{10}$$

which conserves the toroidal momentum. The time step size, τ should be selected to ensure an energy conservation during each time step.

C. Hamiltonian equations of motion

The guiding-center motions of the test particles are calculated by Hamiltonian equations of motion. In order to derive

orbit equations in the non-axisymmetry, it is convenient to use four variables of three dimensional spatial coordinates on the flux coordinates and the pitch. We start from Boozer coordinates,[22] by which the magnetic field is expressed as

$$\vec{B} = \frac{\mu_0}{2\pi}[G(\psi)\vec{\nabla}\phi + I(\psi)\vec{\nabla}\theta + \beta_*(\psi,\theta,\phi)\vec{\nabla}\psi], \quad (11)$$

where μ_0 is the permeability of free space, $G(\psi)$ and $I(\psi)$ are the poloidal and the toroidal current, respectively. The drift Lagrangian is written as

$$L = \frac{1}{2}mv_\parallel^2 + \frac{q}{2\pi}(\psi\dot{\theta} - \chi\dot{\phi}) - \mu B - q\Phi, \quad (12)$$

where q is the electric charge and Φ is the potential. The canonical momenta are

$$p_\theta = \frac{mv_\parallel}{2\pi B}\mu_0 I + \frac{q\psi}{2\pi} = \frac{q}{2\pi}(\mu_0 I\rho_\parallel + \psi), \quad (13)$$

$$p_\phi = \frac{mv_\parallel}{2\pi B}\mu_0 G - \frac{q\chi}{2\pi} = \frac{q}{2\pi}(\mu_0 G\rho_\parallel - \chi), \quad (14)$$

where $\rho_\parallel$ is the parallel gyroradius defined by $\rho_\parallel = mv_\parallel/qB$. Then, the drift Hamiltonian is written as

$$H = \frac{1}{2}mv_\parallel^2 + \mu B + q\Phi = \frac{q^2B^2}{2m} + \mu B + q\Phi. \quad (15)$$

The orbit equations of motion in terms of $(\theta,\phi,p_\theta,p_\phi)$ are obtained from $\dot{\theta} = \frac{\partial H}{\partial p_\theta}$, $\dot{\phi} = \frac{\partial H}{\partial p_\phi}$, $\dot{p_\theta} = \frac{\partial H}{\partial \theta}$, and $\dot{p_\phi} = \frac{\partial H}{\partial \phi}$.[20]

Then, a set of orbit equations as a function of $(\psi,\theta,\phi,\rho_\parallel)$[23] can be obtained throughout the coordinate transforms and can be expressed as

$$\dot{\theta} = -\frac{1}{J}\left[\left(\frac{\partial H}{\partial \rho_\parallel}\right)_\psi\left(\frac{\partial p_\phi}{\partial \psi}\right)_{\rho_\parallel} - \left(\frac{\partial p_\phi}{\partial \rho_\parallel}\right)_\psi\left(\frac{\partial H}{\partial \psi}\right)_{\rho_\parallel}\right]_{\theta,\phi}, \quad (16)$$

$$\dot{\phi} = -\frac{1}{J}\left[\left(\frac{\partial H}{\partial \psi}\right)_{\rho_\parallel}\left(\frac{\partial p_\theta}{\partial \rho_\parallel}\right)_\psi - \left(\frac{\partial p_\theta}{\partial \psi}\right)_{\rho_\parallel}\left(\frac{\partial H}{\partial \rho_\parallel}\right)_\psi\right]_{\theta,\phi}, \quad (17)$$

$$\dot{\rho_\parallel} = \frac{1}{J}\left(\frac{\partial p_\phi}{\partial \psi}\right)_{\rho_\parallel,\theta,\phi}\left(\frac{\partial H}{\partial \theta}\right)_{\rho_\parallel,\psi,\phi} - \frac{1}{J}\left(\frac{\partial p_\theta}{\partial \psi}\right)_{\rho_\parallel,\theta,\phi}\left(\frac{\partial H}{\partial \phi}\right)_{\rho_\parallel,\psi,\theta}, \quad (18)$$

$$\dot{\psi} = -\frac{1}{J}\left(\frac{\partial p_\phi}{\partial \rho_\parallel}\right)_{\psi,\theta,\phi}\left(\frac{\partial H}{\partial \theta}\right)_{\rho_\parallel,\psi,\phi} + \frac{1}{J}\left(\frac{\partial p_\theta}{\partial \rho_\parallel}\right)_{\psi,\theta,\phi}\left(\frac{\partial H}{\partial \phi}\right)_{\rho_\parallel,\psi,\theta}, \quad (19)$$

where the Jacobian J is defined as $J = (q/2\pi)^2\mu_0(G + \iota I)$ with the rotational transform ι. The final form of the Hamiltonian equations of motion is given in Ref. 20.

One of primary results of POCA is a single guiding-center orbit motion. POCA reproduces various guiding-center orbits such as passing, barely trapped, and trapped particles depending on the magnetic field, particle energy, and pitch. For instance, Figure 1 presents trajectories of the guiding-center orbit of a single particle in the axisymmetric and non-axisymmetric configurations. The non-axisymmetric perturbation was applied to a typical NSTX plasma by Eq. (30) with $\epsilon = 0.05$. Trapped particle draws a perfect banana orbit in the axisymmetry; however, shifts of the banana bounce points are found in the non-axisymmetry as shown in Figure 1.

D. Numerical implementation

In order to practically solve the Fokker-Planck equation with the δf Monte Carlo method, POCA follows two steps, orbit and collision step. In the orbit step, a number of test particles ($\geq 10^4$) are initially distributed at the home flux surface, ψ_0 where the neoclassical quantities are calculated. Poloidal and toroidal positions are randomly determined by a random number generator in order to distribute the test particles uniformly in the poloidal and toroidal spaces. Initial pitch of each particle is determined to be uniformly distributed in $-1 \leq \lambda \leq 1$. POCA can test any given energy distribution function, but here we only report cases with monoenergetic and Maxwellian distribution. After the initialization, particles' guiding-center motions are solved by the Hamiltonian equations of motion. Fourth order Runge-Kutta scheme is applied for time integration of the Hamiltonian variables. Next, a collision step followed by orbit step updates the particle pitch and calculates $\hat{f}$ with conserving the momentum by Eq. (10).

POCA is a local code. It calculates the neoclassical properties locally at the home flux surface. Thus, it is required to define an annulus representing the home flux surface. The annulus should be narrow but sufficiently wide to ensure that particles do not leave the annulus in several collision times. Particles leaving the annulus are reinserted at the home flux surface with re-generated random variables of ψ,θ,ϕ, and λ to maintain the total particle number. In this work, the annulus width is defined as 10 times of the banana width. After one cycle of orbit and collision step, a new $\hat{f}$ and δf is obtained by $\delta f = f_M\hat{f}$, which is used to calculate the actual neoclassical transport properties. Even though the

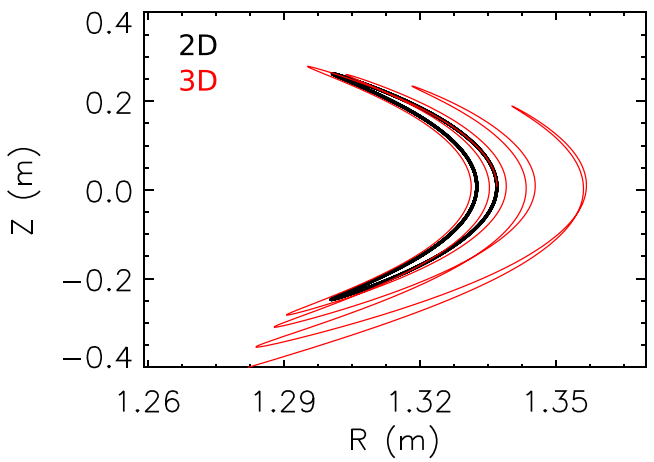

FIG. 1. Trajectories of the guiding-center orbit of a single particle in the axisymmetric (black) and non-axisymmetric (red) configuration. Perfect banana orbit in the axisymmetry is distorted by the non-axisymmetric perturbations, which cause shifts of the banana bounce points.

δf code is much faster than standard Monte Carlo code, computational cost is still expensive. POCA is parallelized by using MPI packages so that the computation speed is significantly enhanced, and this allows a larger number of test particles and/or simultaneous calculations at the multiple flux surfaces. Typically, POCA requires less than half an hour to calculate a single local flux surface with 5×10^4 test particles by using 128 processors.

III. BENCHMARKING ON 2D NEOCLASSICAL TRANSPORT

Various benchmarking tests such as convergence, diffusion, bootstrap current, and momentum conservation are described in this section. Here, axisymmetric configuration is used to compare POCA with neoclassical theories and simulations.

A. Convergence

Convergence of POCA is tested by varying the test particle number. Total number of test particles is the only variable in this benchmarking, while the background plasma conditions and initial energy of test particles are fixed. Figure 2 shows time history of toroidal flow velocity, which is one example of the neoclassical transport property calculated by POCA. It is clearly observed that the flow velocity reaches an asymptotic value in several collision times regardless of the number of test particles. However, the noise significantly decreases as the number of particles increases. This confirms a good convergence feature of POCA when sufficient test particles are used.

B. Diffusion

Diffusions calculated by POCA are benchmarked with ORBIT code,[24] which is well known guiding-center code. Figure 3 shows time history of $\Delta\psi_n^2$, which is a square of displacement of normalized toroidal flux, in the various collision frequencies. Test particles of $5000 \leq N \leq 20\,000$ are initially distributed in the home flux surface to ensure that they are confined in the plasma region for sufficient collision times. Therefore, $\Delta\psi_n^2$ in Figure 3 is an average over N particles. It is observed that the test particles fill a small area at first, which is approximately the banana width, then diffuse in the radial direction as discussed in Ref. 25. Good agreements are found between POCA and ORBIT in the various collision frequencies, which indicate POCA describes the guiding-center motion accurately.

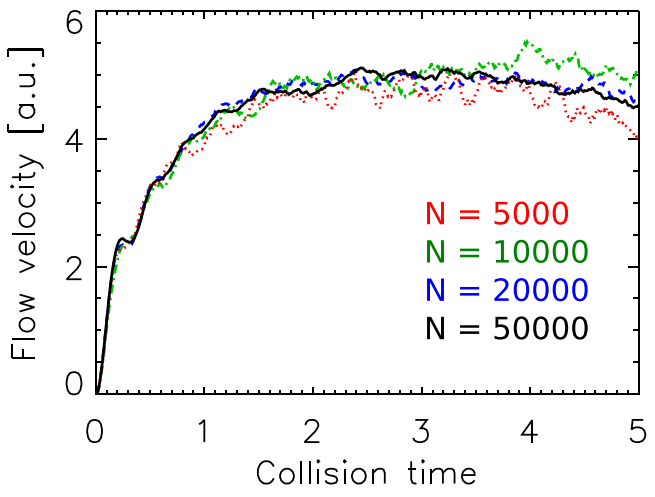

FIG. 2. Time history of toroidal mean velocity with changing the number of test particles. The flow velocity reaches an asymptotic value in several collision times, and it shows better convergence and less noises as the test particle number increases.

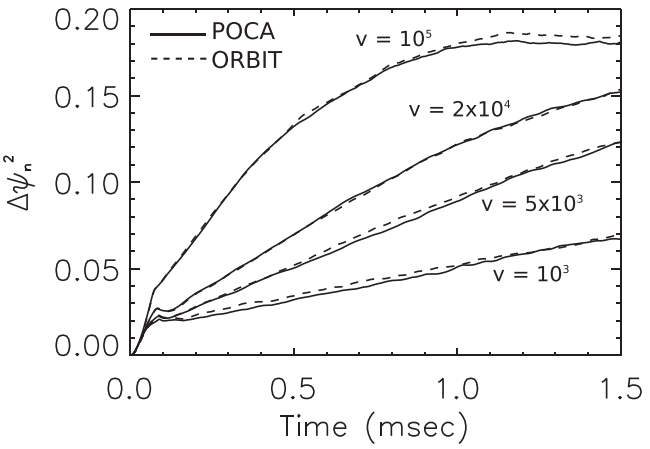

FIG. 3. Time history of particle displacement $\Delta\psi_n^2$ by POCA (solid) compared with ORBIT (dashed) in the various collision frequencies.

For more quantitative comparison, we define a diffusion coefficient of guiding-center as

$$D = \frac{d(\Delta\psi_n^2)}{dt}. \tag{20}$$

The diffusion coefficient by POCA and ORBIT is equivalent to the time derivative of square of particle's displacement, which is the slope of $\Delta\psi_n^2$ after filling the banana width in Figure 3. The diffusion coefficients by POCA also agree very well with ORBIT in the wide range of collision frequencies as shown in Figure 4.

Theoretically predicted Pfirsch-Schlüter, plateau, and banana regimes are observed from Figure 4. Theory predicts

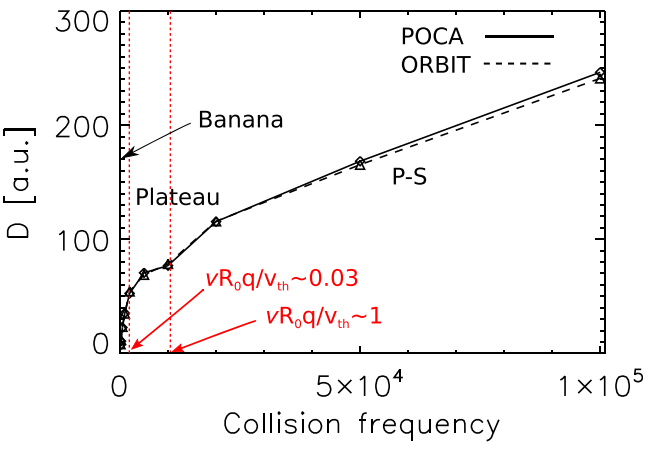

FIG. 4. Calculated diffusion coefficients by POCA (solid) compared to ORBIT (dashed) as a function of collision frequency. The diffusion coefficient defined by a slope of $\Delta\psi_n^2$ shows very good agreement with ORBIT in the wide range of collision frequencies.

the plateau regime exists at $\epsilon^{3/2} \leq \nu R_0 q/v_{th} \leq 1$,[26] where R_0 is the major radius and v_{th} is the thermal speed. Since this benchmarking case considers a high aspect-ratio plasma with $\epsilon \sim 0.1$ and $\epsilon^{3/2} \sim 0.03$, the plateau regime should exist at $400 \leq \nu \leq 10^4$. As indicated in Figure 4, each regime is identified by both POCA and ORBIT consistently with the theory prediction.

C. Bootstrap current

Another benchmarking is performed for ion bootstrap current calculation. The bootstrap current is defined by

$$j_b = \left\langle \frac{j_\parallel}{B} \right\rangle B_0, \tag{21}$$

with $j_\parallel = qu$. The brackets $\langle\rangle$ denote the flux surface average. Figure 5 shows a scaling of the bootstrap current by POCA as a function of collisionality. The collisionality is defined by $\nu_* = \nu q R_0/\epsilon^{3/2} v_{th}$, where ϵ is the inverse aspect-ratio.

Hinton and Rosenbluth[27] found a dependence of the bootstrap current on collisionality in the high aspect-ratio limit as

$$j_b \propto \frac{1}{1+\sqrt{\nu_*}+a\nu_*}, \tag{22}$$

with $a = 0.54$. The result from another δf code[16] indicates a similar dependence of the bootstrap current on collisionality, but $a = 1.44$ from the simulation. Scaling of the bootstrap current agrees well with the predictions from the theory as shown in Figure 5.

D. Momentum conservation

Conservation of the toroidal momentum is critical to separate the non-axisymmetric effect from the axisymmetric one in transport, since it suppresses particle transport induced by collisions and drifts in the axisymmetric configuration. Therefore, the non-ambipolar transport driven by the non-axisymmetric perturbations can be distinguished from the transport driven in the axisymmetry through conserving the toroidal momentum. The easiest way to test the momentum conservation is to check a particle flux across the flux surface in the axisymmetry.[28,29]

The radial particle flux Γ is calculated by

$$\Gamma = \left\langle \int \vec{v_d} \cdot \vec{\nabla}\psi \delta f \, d^3v \right\rangle, \tag{23}$$

where v_d is the drift velocity. The radial particle flux should vanish when it is driven only by like-particle collisions in the axisymmetry since an inward particle flux is generated to conserve the momentum. Figure 6 shows time history of the particle flux in the axisymmetric configuration using the modified momentum conserving operator compared to the non-conserving Lorentz operator. The particle flux using the momentum conserving operator vanishes in several collision times, while a finite flux remains when using the non-conserving operator even in the axisymmetry. Thus, it is confirmed that the modified pitch-angle scattering collision operator used in POCA conserves the toroidal momentum as it should.

IV. NON-AMBIPOLAR TRANSPORT

Axisymmetric magnetic surfaces can be deformed by non-axisymmetric magnetic perturbations. Non-ambipolar transport driven by the non-axisymmetric perturbations is important since a very small perturbation can significantly change the conventional neoclassical transport. In this section, the non-ambipolar particle transport is calculated in a perturbed tokamak, and effects of the magnetic perturbations on transport are discussed.

POCA is developed to easily handle non-axisymmetric magnetic field information. For instance, POCA can read axisymmetric equilibrium from ESC and EFIT, and non-axisymmetric perturbation information from IPEC and

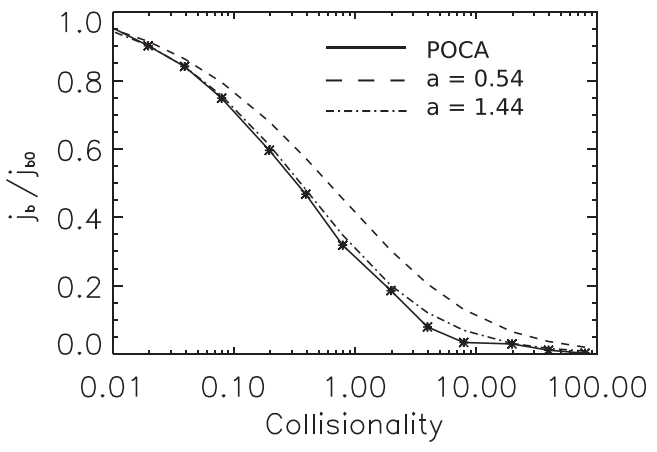

FIG. 5. Scaling of normalized bootstrap current as a function of collisionality. Plotted bootstrap currents are normalized to the bootstrap current at the low collisionality where $\leq 10^{-3}$. POCA calculation shows a good agreement with a theoretical prediction (dashed) and a scaling from another δf code (dashed-dotted).

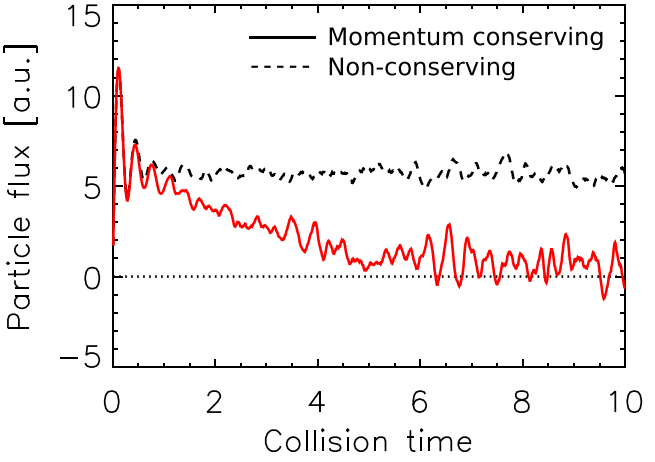

FIG. 6. Time history of radial particle flux using the modified momentum conserving collision operator (solid) and the original Lorentz operator (dashed). The particle flux vanishes when using the momentum conserving collision operator as expected by theory, while a finite flux remains when using the non-conserving operator even in the axisymmetric configuration.

analytic model. Then, the axisymmetric equilibrium field and the non-axisymmetric perturbations are combined to give the total non-axisymmetric magnetic fields as

$$B(\psi,\theta\,\phi) = B_{2D}(\psi,\theta)\left[1+\sum_{mn}\delta_{mn}\cos\left(m\theta-n\phi\right)\right], \quad (24)$$

where δ_{mn} is the strength of the perturbation by a (m,n) mode.

In order to separate a resonant effect from a non-resonant one, an analytic non-axisymmetric perturbation model,

$$B(\psi,\theta\,\phi) = B_{2D}(\psi,\theta)[1+\delta_{mn}\cos\left(m\theta-n\phi\right)] \quad (25)$$

was superimposed to the axisymmetric equilibrium field where $q_0 = 1.05$ and $q_a = 2.8$. ESC equilibrium solver[30] is used to create the axisymmetric equilibrium $B_{2D}(\psi,\theta)$ using a prescribed pressure and safety factor profile. The analytic non-axisymmetric perturbation model applies a single mode which resonates at $q = m/n$ rational surface, thus $m/n = 2/1$ mode resonates at $q = 2$ flux surface in this model. Non-ambipolar particle flux around $q = 2$ flux surface on the model perturbation was calculated by scanning poloidal mode number m from -6 to 10 and fixing toroidal mode number as $n = 1$. Various collision frequencies from 20 to 2000 are selected where $0.012 \le \nu_* \le 1.2$. The normalized non-axisymmetric magnetic perturbation strength (δ_{mn}) is selected to be 0.02 and 0.05. They are stronger than in conventional experiments but useful to show a clear non-axisymmetric effect on the non-ambipolar transport.

Calculation results indicate that the resonant perturbation significantly enhances the non-ambipolar particle flux as shown in Figure 7. The non-resonant perturbations also enhance the particle flux; however, their effects are generally weaker than the resonant one. It is also clear from Figure 7 that the stronger perturbation leads to stronger non-ambiploar transport for both resonant and non-resonant modes. The enhanced non-ambipolar particle flux is directly correlated to the magnetic braking driven by NTV since the non-ambipolar flux is proportional to the NTV torque.[31] The non-ambipolar transport and the resulting NTV transport provide an additional channel for toroidal momentum transport in tokamaks. Experimentally, the modification of toroidal rotation by the magnetic perturbations is called the magnetic braking. Therefore, significant enhancements of the non-ambipolar particle flux by the resonant perturbation clearly indicate a strong resonant nature of magnetic braking, which is typically considered as non-resonant. This trend can be enhanced by plasma response to the magnetic perturbations, which mostly amplifies the resonant modes.

Figure 8 shows the particle flux in the resonant perturbations as a function of collisionality. It is observed that the particle flux increases, reaches a maximum at $\nu_* \sim 0.1$, and then slowly decreases as the collisionality increases. Such a trend is consistent with non-ambipolar transport theory and modeling,[7,32] which might be associated with a bifurcation of the superbanana-plateau and $1/\nu$ regimes. We note that the non-ambipolar transport is very sensitive to a radial electric field. When the electric field exists, the non-ambipolar transport can be complex and enhanced by resonances among the electric field, magnetic precession and/or the bounce frequency. Effects of the radial electric field on the transport is beyond the scope of this study, but will be potentially investigated in the future.

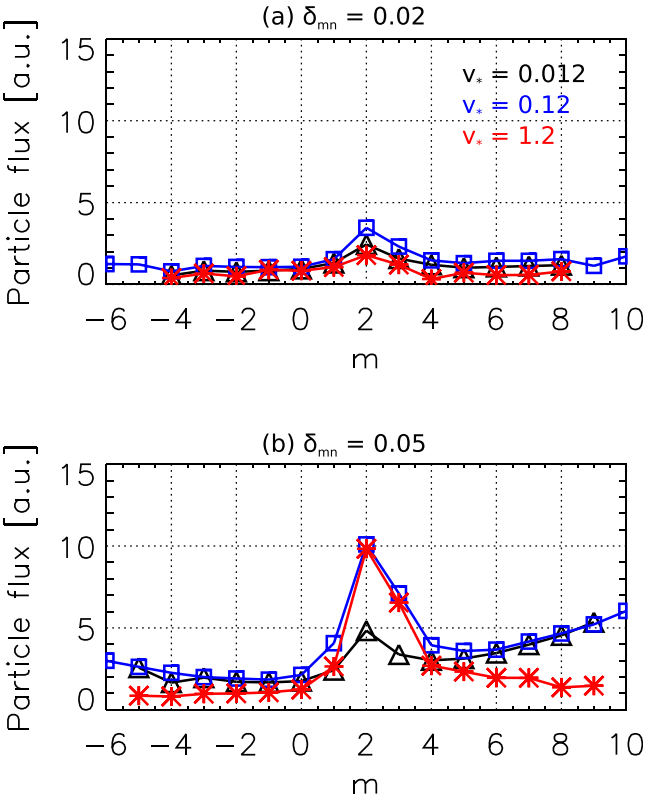

FIG. 7. Non-ambipolar particle flux by $(-6 \le m \le 10, n = 1)$ perturbations around $q = 2$ flux surface for (a) $\delta_{mn} = 0.02$ and (b) $\delta_{mn} = 0.05$. Peak particle fluxes by $(m = 2)$ resonant perturbation clearly indicate resonant nature of magnetic braking, which is typically considered as non-resonant.

V. NEOCLASSICAL TOROIDAL VISCOSITY

POCA can directly calculate the NTV torque. In general, the NTV torque is expressed as $\langle \mathbf{e}_\phi \cdot \nabla \cdot \mathbf{P} \rangle$ with an anisotropic pressure tensor, $\mathbf{P}$ and the toroidal covariant basis,

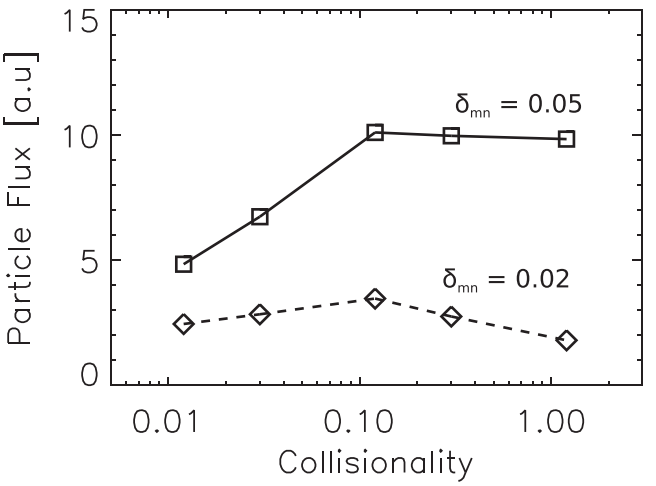

FIG. 8. Non-ambipolar particle fluxes induced by $m/n = 2/1$ resonant perturbation as a function of collsionality. Peaks are found around $\nu_* \sim 0.1$ similarly with theory prediction.

$\mathbf{e}_\phi = \partial\mathbf{x}/\partial\phi$. Since the Jacobian of Boozer coordinates is proportional to B^{-2}, the NTV torque can be expressed in Boozer coordinates as[33]

$$\langle \mathbf{e}_\phi \cdot \nabla \cdot \mathbf{P} \rangle = \left\langle \frac{1}{2}\frac{\partial \delta P}{\partial \phi} \right\rangle = \left\langle \frac{\delta P}{B}\frac{\partial B}{\partial \phi} \right\rangle, \tag{26}$$

where the anisotropic pressure δP is defined by

$$\delta P = \int d^3v \left(\frac{1}{2} m v_\perp^2 + m v_\parallel^2 \right) \delta f, \tag{27}$$

and $\langle\rangle$ denotes the flux surface average. The NTV torque can be calculated with the δf Monte Carlo method throughout calculating the anisotropic pressures and utilizing the spectrum of magnetic perturbations.[34] When expressing the non-axisymmetric magnetic perturbations with Fourier series as

$$\frac{\delta B}{B_0} = \sum_{mn} \delta_{mn}(\psi) \cos(m\theta - n\phi), \tag{28}$$

the NTV torque can be estimated by the following equation:[33–35]

$$\langle \mathbf{e}_\phi \cdot \nabla \cdot \mathbf{P} \rangle = B_0 \sum_{mn} n \delta_{mn} \left\langle \frac{\delta P}{B} \sin(m\theta - n\phi) \right\rangle. \tag{29}$$

Thus, the NTV torque in POCA is a sum of toroidal torques driven by each (m, n) Fourier component of the magnetic perturbations.

The NTV torque calculation by POCA is compared with a generalized combined NTV theory derived from a bounce-averaged drift-kinetic equation[12] as well as $1/\nu$ theory.[10] Circular plasma in the large aspect-ratio is assumed where $R = 10\,\text{m}$, $a = 2.5\,\text{m}$, and $B_0 = 10\,\text{T}$ are chosen for the comparison. A single mode magnetic perturbation is applied, which is expressed as

$$\frac{\delta B}{B_0} = \epsilon \psi_n^2 \cos(7\theta - 3\phi), \tag{30}$$

where ψ_n is the normalized poloidal flux and ϵ is fixed to be 0.02. The perturbation strength $\delta B/B_0$ is a function of radial coordinates so that $\delta B/B_0$ is order of 10^{-4} at the core and 10^{-2} at the edge, which is consistent with a typical NTV experiment.

The kinetic profiles of temperature, density, and safety factor prescribed to construct an axisymmetric equilibrium by ESC are shown in Figure 9. The safety factor profile is modeled by $q(\rho) = 1.2 + 9.8\rho^2$, where ρ is a square root of normalized toroidal flux. Therefore, $m/n = 7/3$ mode resonates at $q = 7/3$ surface around $\psi_n \sim 0.5$ as indicated by a vertical line in Figure 9. This benchmarking case is identical to the FORTEC-3D benchmarking with the same theory in Ref. 32 except that the deuterium species is considered in this paper. Density profile is prescribed as $n(\rho) = n_0(n_1 + n_2 \exp(-n_3\rho^{n_4}))$ with $n_1 = 0.1$, $n_2 = 0.9$, $n_3 = 5.0$, and $n_4 = 4.0$. The density at the magnetic axis, n_0, is varied from 2.5×10^{17} to 2.5×10^{19} while fixing the temperature profile with $T_0 = 0.5\,\text{keV}$. Thus, collisionality is $10^{-2} < \nu_* < 10^{1}$

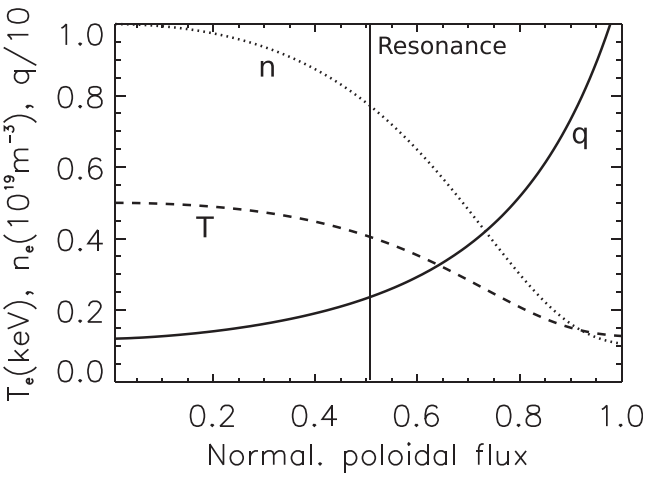

FIG. 9. Kinetic profiles of temperature, density, and safety factor used for benchmarking of the NTV torque. Density profile with $n_0 = 1.0 \times 10^{19}$ is drawn. n_0 is changed for collisionality scan, but the profile shape is the same for every collisionality. Vertical line indicates a resonant flux surface at $q = 7/3$.

depending on the radial positions for each n_0. Note that n_0 is changed for collisionality scan but the density profile shape is the same for every collisionality. The electric potential is currently neglected, thus $E \times B$ rotation is assumed to be zero in this study. The plasmas in this analysis are close to the $1/\nu$ regime depending on the magnetic precession.

We checked δB^2 scaling of NTV, as it is one of fundamental features predicted by NTV theory. The NTV torque by POCA is scaled by the perturbation strength, ϵ when $n_0 = 1.0 \times 10^{19}$. Figure 10 shows the NTV dependence on the perturbation strength at the resonant surface ($\psi_n = 0.5$) and at the non-resonant surfaces ($\psi_n = 0.35, 0.65$). The scaling clearly indicates that the NTV follows the δB^2 dependence at both resonant and non-resonant flux surfaces, which is consistent with the theory prediction.[12,36]

Then, we compare NTV torque profiles by POCA with existing analytic theories. First, POCA is compared to a combined analytic formula[12] in the various collisionalities in Figure 11. Good agreements are found in the overall trend of

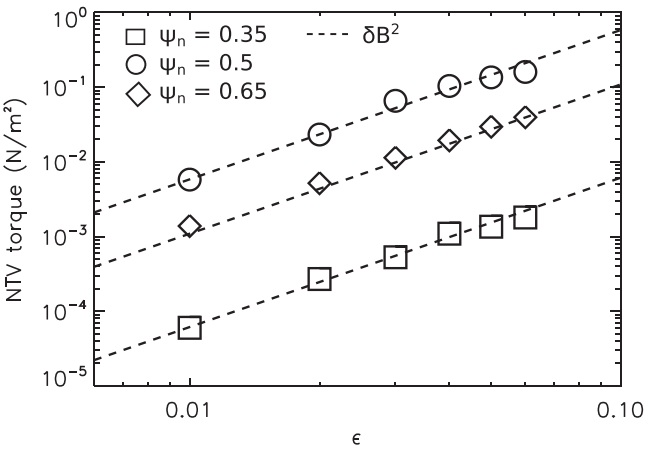

FIG. 10. Dependence of NTV torque on the magnetic perturbation strength. The δB^2 dependence predicted by theory is found by POCA at the resonant and non-resonant flux surfaces.

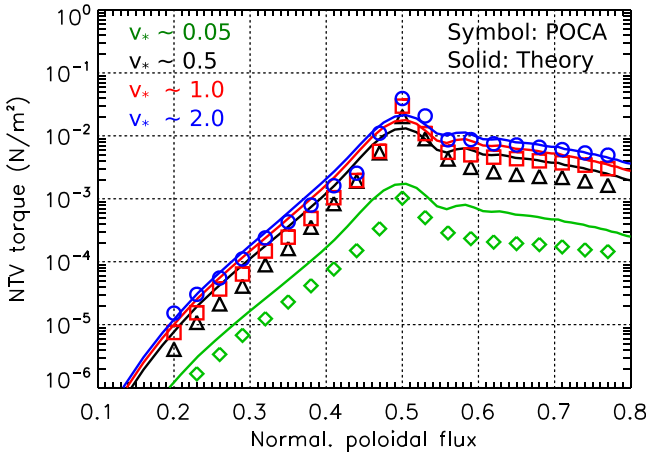

FIG. 11. Comparison of the NTV torque between POCA (symbol) and the combined theory (solid line). Peak NTV torques are clearly observed around the resonant surface at $\psi_n = 0.5$ regardless of collisionality. NTV torques are rapidly reduced at the non-resonant surfaces. The shapes of NTV profiles show good agreements with the theory, but there are discrepancies in amplitudes depending on collisionality, in particular, in the low collisionality regime.

profiles, and the amplitudes agree reasonably well within a factor of 2 depending on collisionality. Note that Maxwellian energy distribution is selected for the test particle energy distribution, thereby high energy particle effects in the Maxwellian tails are taken into account in the POCA calculations. Peak NTV torques nearby resonant flux surface indicates a clear resonant nature of the magnetic braking driven by NTV transport regardless of collisionality. Biggest discrepancy is found in the low collisionality case where the collision frequency is less than 30, but very good agreements are found in the high collisionality cases. Discrepancies depending on the collisionality can be explained by different collision models used in the combined theory and POCA. As previously described, POCA uses the pitch-angle scattering collision operator conserving momentum, while the combined analytic theory uses Krook collision operator which is less accurate in the low collision frequency. This consistently explains the improved agreements in the high collisionality, where the Krook model becomes accurate.

Second, we compare the NTV profiles with Shaing's $1/\nu$ theory.[10] The $1/\nu$ theory uses a pitch-angle scattering collision model but is approximated by separating regimes with collisionality. NTV profiles by POCA, combined formula, and $1/\nu$ formula in the low and high collisionalities are presented in Figure 12. The $1/\nu$ formula predicts stronger resonance and weaker non-resonance of NTV in the low collisionality. On the other hand, POCA and the combined formula predict milder resonance and broader NTV profiles than the $1/\nu$ formula. In the high collisionality, POCA and the combined formula approach $1/\nu$ formula, and a good agreement is found among them at the resonant flux surface. This implies all models consistently describe the resonant feature of the NTV transport. However, discrepancies still remain at the non-resonant flux surfaces even in the high collisionality. This might be caused by the regime separation of the $1/\nu$ formula. Technically, regimes are always overlapping even at a single flux surface due to different pitch-angle

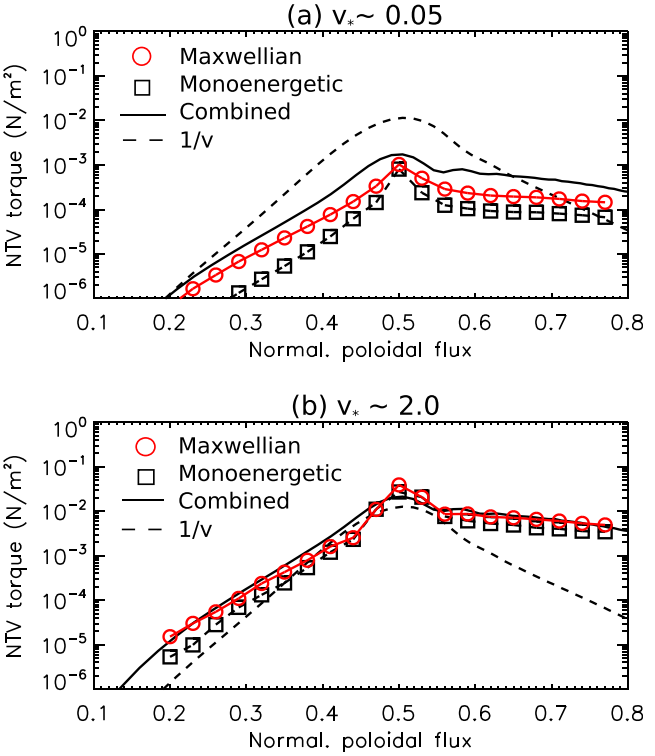

FIG. 12. Comparison of the NTV torque by POCA using Maxwellian and monoenergetic energy distribution with the combined and $1/\nu$ theory in the (a) low and (b) high collisionalities. POCA and the combined formula approach $1/\nu$ formula as the collisionality increases.

and energy of particles. Since the combined formula and POCA take into account the Maxwellian energy distribution without separating regimes, the collisionality varies depending on the energy distribution, and the regimes overlap at the flux surface unlike the $1/\nu$ theory. This may explain the disagreements, especially at the edge where the collision frequency is lower than the core by up to 30% in this benchmarking case.

Note that the Maxwellian energy distribution predicts larger NTV torques than monoenergetic one as shown in Figure 12. The high energy particles in the Maxwellian tails strongly impact on NTV transport, especially at the non-resonant flux surfaces, and their effects are relatively small in the resonant perturbations. In the high collisionality, collisional effects are found to become more dominant than the high energy particle effects both in the resonant and non-resonant magnetic perturbations.

Throughout the various benchmarking tests, it is shown POCA reflects an essential physics of the NTV transport such as δB^2 dependence and the resonant peak, consistently with the theories. In addition, more realistic physics models and numerical conveniences embedded in POCA are beneficial for the NTV analysis in the future.

VI. SUMMARY

A new δf particle orbit code, POCA has been developed to calculate the neoclassical transport in perturbed tokamaks. POCA employs a δf Monte Carlo method with the modified Lorentz collision operator conserving the toroidal momentum.

Neoclassical transport properties such as diffusion and bootstrap current were successfully benchmarked in the axisymmetric configuration. Non-axisymmetric neoclassical transports such as non-ambipolar particle flux and NTV torque were calculated and compared with the theories using an analytic non-axisymmetric perturbation model. POCA demonstrated the clear resonant nature of the non-ambipolar transport, NTV, and thus magnetic braking. The successful benchmarking results support that POCA can be applicable to experimental and theoretical studies on the non-ambipolar transport in perturbed tokamaks, thanks to its accuracy and computational benefits.

ACKNOWLEDGMENTS

The author K. Kim would like to thank Roscoe White for benchmarking with ORBIT code and Stephane Ethier for parallelization of POCA. The private communication with Seung-Hoe Ku and Ahmed Diallo was a great help. This work was supported by DOE Contract No. DE-AC02-09CH11466.

[1]A. A. Galeev, R. Z. Sagdeev, H. P. Furth, and M. N. Rosenbluth, Phys. Rev. Lett. **22**, 511 (1969).
[2]R. J. Goldston, R. B. White, and A. H. Boozer, Phys. Rev. Lett. **47**, 647 (1981).
[3]K. Ikeda, Nucl. Fusion **47**, S1 (2007).
[4]T. E. Evans, R. A. Moyer, P. R. Thomas, J. G. Watkins, T. H. Osborne, J. A. Boedo, E. J. Doyle, M. E. Fenstermacher, K. H. Finken, R. J. Groebner, M. Groth, J. H. Harris, R. J. La Haye, C. J. Lasnier, S. Masuzaki, N. Ohyabu, D. G. Pretty, T. L. Rhodes, H. Reimerdes, D. L. Rudakov, M. J. Schaffer, G. Wang, and L. Zeng, Phys. Rev. Lett. **92**, 235003 (2004).
[5]S. A. Sabbagh, R. E. Bell, J. E. Menard, D. A. Gates, A. C. Sontag, J. M. Bialek, B. P. LeBlanc, F. M. Levinton, K. Tritz, and H. Yuh, Phys. Rev. Lett. **97**, 045004 (2006).
[6]A. M. Garofalo, K. H. Burrell, J. C. DeBoo, J. S. deGrassie, G. L. Jackson, M. Lanctot, H. Reimerdes, M. J. Schaffer, W. M. Solomon, and E. J. Strait, Phys. Rev. Lett. **101**, 195005 (2008).
[7]J. D. Callen, Nucl. Fusion **51**, 094026 (2011).
[8]W. Suttrop, T. Eich, J. C. Fuchs, S. Günter, A. Janzer, A. Herrmann, A. Kallenbach, P. T. Lang, T. Lunt, M. Maraschek, R. M. McDermott, A. Mlynek, T. Pütterich, M. Rott, T. Vierle, E. Wolfrum, Q. Yu, I. Zammuto, H. Zohm, and ASDEX Upgrade Team, Phys. Rev. Lett. **106**, 225004 (2011).
[9]A. H. Boozer, Phys. Fluids **23**, 2283 (1980).
[10]K. C. Shaing, Phys. Plasmas **10**, 1443 (2003).
[11]K. C. Shaing, P. Cahyna, M. Becoulet, J.-K. Park, S. A. Sabbagh, and M. S. Chu, Phys. Plasmas **15**, 082506 (2008).
[12]J.-K. Park, A. H. Boozer, and J. E. Menard, Phys. Rev. Lett. **102**, 065002 (2009).
[13]Y. Sun, Y. Liang, K. C. Shaing, H. R. Koslowski, C. Wiegmann, and T. Zhang, Phys. Rev. Lett. **105**, 145002 (2010).
[14]A. J. Cole, J. D. Callen, W. M. Solomon, A. M. Garofalo, C. C. Hegna, M. J. Lanctot, H. Reimerdes, and DIII-D Team, Phys. Rev. Lett. **106**, 225002 (2011).
[15]S. E. Parker and W. W. Lee, Phys. Fluids B **5**, 77 (1993).
[16]M. Sasinowski and A. H. Boozer, Phys. Plasmas **2**, 610 (1995).
[17]J.-K. Park, A. H. Boozer, and A. H. Glasser, Phys. Plasmas **14**, 052110 (2007).
[18]M. N. Rosenbluth, R. D. Hazeltine, and F. L. Hinton, Phys. Fluids **15**, 116 (1972).
[19]A. H. Boozer and H. J. Gardner, Phys. Fluids B **2**, 2408 (1990).
[20]M. Sasinowski and A. H. Boozer, Phys. Plasmas **4**, 3509 (1997).
[21]A. H. Boozer and G. Kuo-Petravic, Phys. Fluids **24**, 851 (1981).
[22]A. H. Boozer, Phys. Fluids **24**, 1999 (1981).
[23]R. B. White, Phys. Fluids B **2**, 845 (1990).
[24]R. B. White and M. S. Chance, Phys. Fluids **27**, 2455 (1984).
[25]D. A. Gates, H. E. Mynick, and R. B. White, Phys. Plasmas **11**, L45 (2004).
[26]J. Wesson, *Tokamaks* (Oxford University Press, New York, 1997).
[27]F. L. Hinton and M. N. Rosenbluth, Phys. Fluids **14**, 836 (1973).
[28]Z. Lin, W. M. Tang, and W. W. Lee, Phys. Plasmas **2**, 2975 (1995).
[29]A. Bergmann, A. G. Peeters, and S. D. Pinches, Phys. Plasmas **8**, 5192 (2001).
[30]L. E. Zakharov and A. Pletzer, Phys. Plasmas **6**, 4693 (1999).
[31]K. C. Shaing, Phys. Fluids **26**, 3315 (1983).
[32]S. Satake, J.-K. Park, H. Sugama, and R. Kanno, Phys. Rev. Lett. **107**, 055001 (2011).
[33]J. L. V. Lewandowski, J. Williams, A. H. Boozer, and Z. Lin, Phys. Plasmas **8**, 2849 (2001).
[34]J. D. Williams and A. H. Boozer, Phys. Plasmas **10**, 103 (2003).
[35]S. Satake, H. Sugama, R. Kanno, and J.-K. Park, Plasma Phys. Controlled Fusion **53**, 054018 (2011).
[36]J.-K. Park, Phys. Plasmas **18**, 110702 (2011).